Catalysis Science & Technology

Accepted Manuscript

ROYAL SOCIETY OF CHEMISTRY

www.rsc.org/catalysis

Catalysis Science and Technology RSCPublishing

ARTICLE

Ceria Promotion of Acetaldehyde Photo-oxidation in a TiO_2-based Catalyst: a Spectroscopic and Kinetic Study

Cite this: DOI: 10.1039/xoxxoooooox

Received ooth January 2012,
Accepted ooth January 2012

DOI: 10.1039/xoxxoooooox

www.rsc.org/

M. J. Muñoz-Batista,[a] M. M. Ballari,[b] A. E. Cassano,[b] O. M. Alfano,[b,*] A. Kubacka,[a,*] Marcos Fernández-García[a]

A spectroscopic and kinetic study of the photo-oxidation of acetaldehyde with a CeO_2-TiO_2 composite catalyst is presented. Both UV and Visible illumination conditions were tested. The study focuses on analysing the role of ceria in the photocatalytic behaviour by contrasting the CeO_2-TiO_2 behaviour with the appropriate TiO2 reference. To this end, we developed an intrinsic kinetic expression with explicit inclusion of the effect of photon absorption on the reaction rate as well as a reaction scheme proposed on the basis of a joint Diffuse Reflectance Infrared Fourier Transform Spectroscopy (DRIFTS) and Electron Paramagnetic Resonance (EPR) characterization. Combination of spectroscopic and kinetic tools provides quantitative evidence that the oxide-oxide contact controls activity in the composite catalyst through the number of hole-related species able to attack the pollutant, this in turn being related to ceria defects influence on charge carrier fate. The above mentioned key properties controlling photoactivity are the same for UV or visible excitation, rendering a highly active photocatalyst, suitable for sunlight applications.

1. Introduction

Volatile organic compounds (VOCs) are present in the atmosphere as a result of being solvent in numerous industrial processes such as dry cleaning, plastic manufacturing and fumigation, as well as from emission of automobile engines and/or buildings.[1] The toxicity and carcinogenic character of a significant number of these molecules as well as their persistence in the media have triggered the search of technologies for their elimination.

Photocatalysis is among the most studied technologies in VOCs elimination.[2,3,4] Photocatalysis has inherent advantages with respect to other technologies as is carried out at ambient temperature and pressure and using oxygen from air as oxidant. A weak point, however, is the fact that the most active single phase is based on the anatase phase of titania.[2-5] All titania polymorphs are UV absorbers and anatase displays a relatively wide band gap of ca. 3.0-3.4 eV, requiring UV light for triggering photo-based reactions. The need of using a renewable energy source such as the sun as energetic source of photocatalytic reactions has promoted a wealth of research, mostly based in the modification of titania. Such research aims to obtain highly active and universal, i.e. able to eliminate pollutants independent of their chemical nature, materials.[2-6] Among the most useful possibilities, the use of ceria as a surface phase in contact with anatase has received significant attention.[7,8,9,10,11,12,13,14,15,16,17,18,19,20] In these systems, the ceria-titania interface has been shown to play an important role.[17]

In this contribution we aim to provide evidence of the mechanism and kinetics of the acetaldehyde photo-oxidation using a CeO_2-TiO_2 catalyst. Acetaldehyde is a model pollutant which has been used frequently to test the activity of titania based photocatalysts.[19-21] Applying an efficiency analysis through calculation of the quantum (or true) yield of the reaction, we spotted out that the ceria promotion of titania activity is maximized with a 2.5 mol. % content of the former oxide. This maximum occurs under both UV and visible light excitation, indicating the suitability of the CeO_2-TiO_2 system for sunlight-type applications.[20] Moreover, rather high activity is obtained both for UV and visible light excitation while eliminating polar or non-polar gas-phase pollutants with the 2.5 mol. % CeO_2-TiO_2 formulation, overperfoming titania single phase references (including nano-anatase and P25) by factors exceeding 2.5. This indicates the goodness of the CeO_2-TiO_2 system for general VOC elimination.[17,18,19]

Through a combined catalytic and spectroscopic study of the mechanism and kinetics of the acetaldehyde photo-oxidation, this contribution attempts to interpreting such a good performance and unveiling its physico-chemical roots. Two illumination conditions, UV and visible, were considered. To this end, here we first developed an intrinsic kinetic formulation which consider all experimental variables affecting photoactivity, i.e. light intensity, pollutant concentration and humidity level. Only an intrinsic kinetic expression of the reaction rate obtained within a framework involving the mass balances of the reacting species and the evaluation of the radiation field in the employed reaction provides

information valid for general use. Note that such kinetic modelling requires a mechanistic sequence usually based in previous works.[22,23] The present approach uses spectroscopic tools to provide a self-consistent approach. With time-resolved infrared spectroscopy we will evaluate the initial steps of the mechanism while the whole mechanism reliability is tested with the help of electron paramagnetic resonance (EPR).[17] With the last spectroscopy, we attempt to provide evidence of the radical species involved in the rate determining step(s) of the mechanism.[24,25,26] Confrontation of the photo-oxidation rates obtained under kinetic regime as a function of two observables, the kinetic constants evaluated by the modelling and a normalized (by light-intensity) EPR rate of radical species, will show key information concerning the mechanism and kinetics of the reaction as well as a way to understand the main physico-chemical parameters acting on photocatalytic performance.

2. Experimental

2.1. Catalyst preparation

Materials were prepared using a microemulsion preparation method using *n*-heptane (Scharlau) as organic media, Triton X-100 (Aldrich) as surfactant and hexanol (Aldrich) as cosurfactant. The TiO_2 sample was obtained as a first step using a microemulsion into the aqueous phase and titanium tetraisopropoxide as precursor. The composite sample with 2.5 molar % of CeO_2 regarding 1 % molar of TiO_2 ($0.025CeO_2/TiO_2$) was obtained using cerium nitrate (Alfa Aesar) as precursor of ceria which was introduced in the aqueous phase of a microemulsion. After 30 min of agitation, a stoichiometric (to obtain the corresponding Ce(III) hydroxide) quantity of tetramethyl-ammonium-hydroxide (TMAH) was introduced from the aqueous phase of a similar microemulsion. After 5 min, titanium tetra-isopropoxide was introduced into the previously resulting microemulsion drop by drop from a mixture with isopropanol (2:3). Water/Ti and water/surfactant molar ratios were, respectively, 110 and 18 for all samples.[27,28] The resulting mixture was stirred for 24 h, centrifuged, and the separated solid precursors rinsed with methanol and dried at 110 ^{o}C for 12h. After drying, the solid precursors were subjected to a heating ramp (2 ^{o}C min^{-1}) up to 500 ^{o}C, maintaining this temperature for 2 h.

2.2. EPR and Infrared measurements

The EPR measurements were done with a Bruker ER200D spectrometer operating in the X band and calibrated with a 2,2-diphenyl-1-picrylhydrazyl (DPPH) standard. For the 5,5-dimethyl-1-pyrroline N-oxide (DMPO) spin-trapping EPR experiments, the samples were suspended in water at a concentration of 0.6 g L^{-1} and sonicated for 4 min. A 0.01 M aqueous solution of the DMPO spin trap (supplied by Sigma) was prepared and kept on ice during the whole set of experiments. Bid stilled water (Elix-10) was employed for these preparations. The solid suspension (100 µL) and the DMPO solution (100 µL) were mixed into an EPR flat quartz cell under atmospheric air and irradiated for different times through a spectroscopic Pyrex glass filter with a cut off at ca. 220 nm. The cell was then immediately transferred to the spectrometer cavity for EPR analysis. A small decay of the radical concentration (ca. 5% on average) was observed in the dark during the course of spectrum recording. The spectra were obtained at 298 K at a microwave frequency of ca. 9.75 GHz, a microwave power of 19.5 mW, a modulation frequency of 100 kHz, modulation amplitude of 1 G, and a spectrometer gain of 2×10^5. No significant signal saturation was observed under those conditions. Blank experiments were also performed over mixtures of 100 µL of the DMPO solution and 100 µL of water to confirm the absence of radical formation in the absence of the solid under the employed conditions. The in-situ light excitation was carried out using two fluorescent UV (Sylvania 6W F6WBLT-65) or Visible (Sylvania 6W F6W/D) lamps symmetrically positioned on each side of the cell (See Fig. S1 of the supporting information).

Diffuse Reflectance Infrared Fourier Transform Spectra (DRIFTS) were taken in a Bruker Vertex 80 FTIR spectrometer using a MCT detector and running under OPUS/IR software. The set-up consists of a praying mantis DRIFTS accessory (Harrick Scientific) and a reaction cell (HVC, Harrick Scientific). The reaction mixture was prepared by injecting acetaldehyde (≥99%; Aldrich) into a wet (ca. 45% relative humidity) 20 vol.% O_2/N_2 flow before entering the DRIFTS cell. The DRIFTS spectra were collected in the range of 4000–600 $cm^{-1}$with a resolution of 2 cm^{-1}, by averaging 10 scans over a total of 1.2 seconds.

In DRIFTS experiments in-situ light excitation was carried out using 365/488 nm (20 nm half-width) radiation with an intensity of ca. 12/10 mW cm^{-2}. These conditions are close (both in average wavenumber and intensity of the light) to the UV/Visible illumination conditions at the photoreactor.

2.3. Reactor system and experimental conditions

Fig.1 provides a scheme of the used apparatus to study the photodegradation of acetaldehyde in gas phase. The corresponding amount of catalyst was suspended in 2 mL of ethanol, painted on a borosilicate plate and dried at RT. The reaction chamber was confined between two rectangular acrylic windows (20 × 9.5 cm^2). Each catalytic plate was exposed to the radiation coming from two sets of seven UV (Philips TL 4W/08 F4T5/BLB) or Visible (General Electric GE F4T5/CW) emitting lamps; each set faced one sample plate side. The lamps in each set were arranged with a separation between axes of 2.6 cm, and the distance from them to the reactor center plane was 4.3 cm. Acetaldehyde was used as the pollutant supplied from a cylinder containing 300 ppm of acetaldehyde in nitrogen. The acetaldehyde was mixed with streams of air and water-saturated air to obtain the concentration and relative humidity required (20 ppm and 45% respectively). The flow rates of reactive gases were controlled by online mass-flow controllers (Matheson Corp.). The total flow rate of the reaction mixture was 1000 mL min^{-1}. The temperature and the humidity of the feed stream were measured with an online thermo-hygrometer located before the inlet

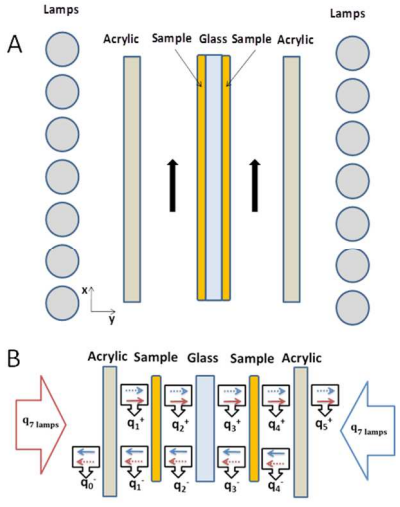

Fig.1. A. Scheme of the photocatalytic reactor. B. Schematic representation of the radiation balance. Solid arrow: transmitted radiation flux; dotted arrow: reflected radiation flux

point of photoreactor. The concentration of the reactants and products was analyzed using offline gas chromatography (Hewlett-Packard 5890 Series II; J &W Scientific INC. DB-1301column; FID detector) performing a direct injection of the gas sample.
Experiments were performed with different acetaldehyde concentrations, relative humidity and irradiation levels, using 3 levels for each factor according to Box–Behnken design. Note that, for the reaction under UV irradiation it was necessary to use irradiation levels lower than 25 %. They made negligible the diffusive resistances and allowed working under kinetic control regime in all conditions tested here. Steady state conditions are achieved in relativity short reaction time (see Fig. S1 at the Supporting Information section). Full experimental details are given in Table 1.

Table 1. Experimental operating conditions

Operating Conditions	Unit	Value
Flow rate	$cm^3\ min^{-1}$	1000
Temperature	°C	25
Pressure	atm	1
Inlet concentration	ppm	10, 20, 30
Relative humidity	%	10, 45, 70
Irradiation level for UV reactions	%	9, 13, 25
Irradiation level for Visible reactions	%	35, 50, 100
UV incident Irradiance[a]	$W\ cm^{-2}$	4.02×10^{-3}
Visible incident Irradiance[a]	$W\ cm^{-2}$	6.62×10^{-3}

[a] Measured at center of the reactor

3. Kinetic and Radiation model

3.1. Mass Balance

According to the photoreactor geometry (Fig. 1A), under kinetic control regime (note that external and internal mass transfer are negligible; see details in the Supporting Information) and taking into account the following assumptions; (i) the reactor operates under steady state conditions, (ii) the convective flow exists only in the axial coordinate x, (iii) negligible axial diffusion when compared to the convective flux in that direction), and (iv) negligible homogeneous photochemical reactions, acetaldehyde mass balance follows the differential mass transfer Eq. (1).[29,30]

$$v_x\left(\frac{dC_{CH_3CHO}}{dx}\right) = a\, r_{CH_3CHO} \quad (1)$$

The boundary condition necessary to solve this differential equation is given by: $C_{CH_3CHO}(\mathrm{x}=0) = \mathrm{C}_{\mathrm{C_{CH_3CHO}},\mathrm{in}}$, which is measured experimentally; where r_{CH_3CHO} and C_{CH_3CHO} are the average reaction rate and concentration of acetaldehyde, respectively. a,v_x and x are the external catalytic surface area per unit volume, the average axial velocity and the axial coordinate, respectively.

3.2. Kinetic model

The mechanism of any photochemical process is usually complex because the excited states of the molecules give different kinds of reactions. However, the kinetic mechanism can be simplifying take into account the well-established initial steps of any photocatalytic processes:(i) the photo-excited sample generates electrons and holes, (ii) holes may react with adsorbed water and superficial OH^- ions to generate hydroxyl radicals, and (iii) molecular oxygen acts as an acceptor species in the electron-transfer reaction, partly reducing recombination processes and the resulting loss of energy as heat.[17,29,30,31,,32]According to the literature, (iv) the acetaldehyde molecule can be initially attacked by hydroxyl radicals, forming several intermediates up to the eventual formation of CO_2.[33,34]Also, the acetaldehyde molecule and other intermediates can be attacked by photo-generated holes (direct pathway) but is accepted that the $OH^\bullet$ pathways is significantly faster than the hole one. Table 2 present the basic reaction scheme used to develop the intrinsic kinetic expression. Such scheme will be justified in subsequent sections.

Table 2. Simplified reaction scheme

No.	Reaction step	Reaction rate
0	$Cat + h\nu \rightarrow Cat + h^+ + e^-$	rg
1	$h^+ + H_2O_{ads} \rightarrow OH^{\cdot} + H^+$ $h^+ + OH^-_{ads} \rightarrow OH^\bullet$	$k_1[H_2O]_{ads}[h^+]$
2	$e^- + O_{2\ ads} \rightarrow O_2^{\cdot-}$	$k_2[O_2]_{ads}[e^-]$
3	$h^+ + e^- \rightarrow heat$	$k_3[h^+][\,e^-]$
4	$CH_3CHO_{ads} + OH^{\cdot} \rightarrow Products$	$k_4[CH_3CHO]_{ads}[OH^\bullet]$
5	$OH^\bullet + OH^- \rightarrow O^{\bullet-} + H_2O_{ads}$	$k_5[OH^\bullet][\,OH^-]$

The acetaldehyde degradation rate can be expressed as Eq. 2.

$$r_{CH_3CHO} = -k_4[CH_3CHO]_{ads}[OH^\bullet] \quad (2)$$

The steady-state approximation may be applied to the net generation rates of free hydroxyl radical and holes:

$$rOH^\bullet = k_1[H_2O]_{ads}[h^+] - k_4[CH_3CHO]_{ads}[OH^\bullet] - k_5[OH^\bullet][\,OH^-] \approx 0 \quad (3)$$

$$[OH^\bullet] = \frac{k_1[H_2O]_{ads}[h^+]}{k_4[CH_3CHO]_{ads} + k_5[OH^-]} \quad (4)$$

$$rh^+ = rg - k_1[H_2O]_{ads}[h^+] - k_3[h^+][\,e^-] \approx 0 \quad (5)$$

Eq. 5 can be simplified considering that charge recombination in semiconductors is expected to be much faster than any chemically related charge transfer step ($k_3[h^+][e^-] \gg k_1[H_2O]_{ads}[h^+]$).[17,35,36] Furthermore, under equilibrium conditions, the concentration of holes and electrons can be considered approximately equal and constant, then:

$$[h^+] = \sqrt{\frac{rg}{k_3}} \quad (6)$$

Replacing Eq. (6) into Eq. (4) and subsequently into the acetaldehyde degradation rate equation (Eq. 2) and considering $k_5[OH^-] = cte = \gamma$ (kinetic constant corresponding to the scavenging effect of $OH^\bullet$ radicals)[37,38]

$$r_{CH_3CHO} = -\frac{k_4[CH_3CHO]_{ads}k_1[H_2O]_{ads}}{k_4[CH_3CHO]_{ads} + \gamma}\sqrt{\frac{rg}{k_3}} \quad (7)$$

The surface concentrations of adsorbed acetaldehyde and water can be obtained from the balance of active sites. Considering that acetaldehyde and water compete for the same adsorption sites, the relation between the surface concentration and gas-phase concentrations is given by Eqs. (8) and (9).

$$[H_2O]_{ads} = \frac{K_{H_2O}[Sites]C_{H_2O}}{1 + K_{H_2O}C_{H_2O} + K_{CH_3CHO}C_{CH_3CHO}} \quad (8)$$

$$[CH_3CHO]_{ads} = \frac{K_{CH_3CHO}[Sites]C_{CH_3CHO}}{1+ K_{H_2O}C_{H_2O}+K_{CH_3CHO}C_{CH_3CHO}} \quad (9)$$

Replacing Eqs. (8) and (9) into Eq. (7)

$$r_{CH_3CHO} = -\frac{k_4K_{CH_3CHO}[Sites]C_{CH_3CHO}k_1K_{H_2O}[Sites]C_{H_2O}}{\gamma(1+ K_{H_2O}C_{H_2O}+K_{CH_3CHO}C_{CH_3CHO})\left(\frac{k_4K_{CH_3CHO}[Sites]C_{CH_3CHO}}{\gamma}+ (1+ K_{H_2O}C_{H_2O}+K_{CH_3CHO}C_{CH_3CHO})\right)}\sqrt{\frac{rg}{k_3}} \quad (10)$$

The local superficial rate of electron-hole pair generation (rg) is given by:

$$rg = \int_\lambda \phi_\lambda e_\lambda^{a,s}(x,y,z)d\lambda = \overline{\phi}\sum e_\lambda^{a,s}\ (x,y,z) \quad (11)$$

Substituting Eq. (11) in Eq. (10) and grouping constants, the acetaldehyde degradation rate can be expressed as:

$$r_{CH_3CHO} = -\frac{\alpha_1 C_{CH_3CHO}C_{H_2O}}{(1+ K_{H_2O}C_{H_2O}+K_{CH_3CHO}C_{CH_3CHO})(1+\alpha_2 C_{CH_3CHO}+ K_{H_2O}C_{H_2O}+K_{CH_3CHO}C_{CH_3CHO})}\sqrt{e^{a,s}} \quad (12)$$

where:

$$\alpha_1 = \frac{k_4K_{CH_3CHO}[Sites]k_1K_{H_2O}[Sites]}{\gamma}\sqrt{\frac{\overline{\phi}}{k_3}} \quad (13)$$

$$\alpha_2 = \frac{k_4K_{CH_3CHO}[Sites]}{\gamma} \quad (14)$$

3.3. Radiation model

In order to calculate the local reaction rate (Eq. 12), a radiation field model was developed to predict the Local Superficial Rate of Photon Absorption (LSRPA) at each (x,z) point on the photocatalytic film; Eq. 15 (for right plate) and 16 (for left plate).[20] These equations provide the same value at x,±δy,z (δ → 0) points for the right or left surface of the sample according to the symmetry of the system (see Figs. 1A and 1B).

$$e_\lambda^{a,s}(x,z) = a_{s,\lambda}\, q_{1,\lambda}^{+}(x,z) + a_{s,\lambda}\, q_{2,\lambda}^{-}(x,z) \quad (15)$$

$$e_\lambda^{a,s}(x,z) = a_{s,\lambda}\, q_{4,\lambda}^{-}(x,z) + a_{s,\lambda}\, q_{3,\lambda}^{+}(x,z) \quad (16)$$

The $a_{s,\lambda}$ symbol denotes the spectral fraction of absorbed incident energy by the photocatalytic sample. $q_{1,\lambda}^{+}$,$q_{2,\lambda}^{-}$,$q_{4,\lambda}^{-}$, $q_{3,\lambda}^{+}$ are the net radiation fluxes impinging on each side of the plate according to Fig. 1B.

Using the methodology developed for the system consisting on parallel glass plates,[39] we can express the Eq. 15 (in the specific case of the right plate) in terms of the fraction of incident energy transmitted, reflected and absorbed by acrylic (a), glass (gl) and sample (s) (measured variables) at each point on the catalytic plate.

$$e_\lambda^{a,s}(x,z) = q_\lambda(x,z)T_{a,\lambda}\, a_{s,\lambda}\left(1+\frac{R_{gl,\lambda}T_{s,\lambda}-R_{gl,\lambda}^2R_{s,\lambda}\,T_{s,\lambda}+T_{gl,\lambda}\,T_{s,\lambda}+T_{gl,\lambda}^2R_{s,\lambda}\,T_{s,\lambda}}{1-2R_{gl,\lambda}R_{s,\lambda}+ R_{al,\lambda}^2R_{s,\lambda}^2-T_{al,\lambda}^2R_{s,\lambda}^2}\right) \quad (17)$$

Where the radiation flux on each (lamp set faced) plate side is thus given by Eq. 18, which was obtained using the coordinate system presented in Fig. 2, the three dimensional source with superficial emission model and the ray-tracing computational method.[20]

$$q(x,y,z) = \sum_{L=1}^{L=7}\sum_\lambda \int_{\varphi min,L}^{\varphi max,L}\int_{\Theta min,L}^{\Theta max,L}\frac{P_{\lambda,L}}{2\pi^2R_LZ_L}\sin^2\Theta\,\cos\varphi\, d\varphi d\Theta \quad (18)$$

$P_{\lambda,L}$ is the spectral emission power of the lamp, and R_L and Z_L are the radius and length of the i − th lamp, respectively.

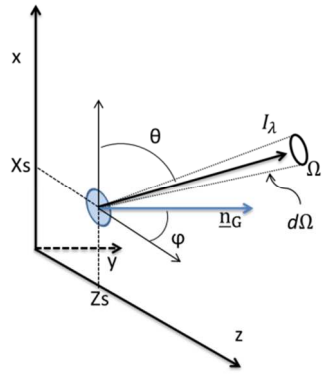

Fig. 2. Coordinate system adopted for the reactor-lamps system

The integration limits for the spherical coordinate (φ and Θ) can be evaluated from the geometry and dimensions of the system and lamps (Figs. 1A and 2). A complete description is presented in the Supporting Information section. To validate the proposed radiation model, radiation fluxes arriving at the catalytic surface were measured with a UV-radiometer. The differences between experimental data and model predictions were 7 and 10 % for UV and visible lamp respectively.[20]

The diffuse transmittance and reflectance of the glass plate (gl), acrylic (a) and catalyst deposited on the plate (s, gl) were measured as a function of the wavelength within the emission range of the lamps. The diffuse transmittance and reflectance of the catalysts can be obtained using Eqs. 19 and 20 (Fig. S2).[20,40]

$$T_{s,\lambda} = \frac{T_{s,gl,\lambda}T_{gl,\lambda}\,(-1+R_{s,gl,\lambda}\,R_{gl,\lambda})}{R_{gl,\lambda}^2T_{s,gl,\lambda}^2-T_{gl,\lambda}^2} \quad (19)$$

$$R_{s,\lambda} = -\frac{-R_{gl,\lambda}T_{s,gl,\lambda}^2 + R_{s,gl,\lambda}T_{gl,\lambda}^2}{R_{gl,\lambda}^2 T_{s,gl,\lambda}^2 - T_{gl,\lambda}^2} \quad (20)$$

The local superficial rate of photon absorption for the samples and the lamp used are presented in the Supporting Information section (Fig. S3).

3.4. EPR model

According to Table 2, more precisely to the reaction step representing the generation of hydroxyl radicals (step 1), the rate for $OH^{\bullet}$ formation in an EPR experiment is given by:

$$r_{OH^{\bullet}} = k_1[H_2O]_{ads}[h^+] \quad (21)$$

Where the hole concentration can be approximated by Eq. 6:

$$\frac{r_{OH^{\bullet}}}{\sqrt{e^{a,v}}} = \sqrt{\frac{\bar{\phi}}{k_3}}k_1[H_2O]_{ads} \quad (22)$$

Using $r_g = \bar{\phi}\sum_\lambda e_\lambda^{a,v}$

Considering that the scattering contribution can be neglected (due to the limited cross section of the cell with respect to the secondary – aggregate- particle size of the catalysts; see dimension details of the EPR cell in the Fig. S4) the Local Volumetric Rate of Photon Absorption at the EPR cell can be obtained using Eq. 23 (Equations for φ and Θ integration limits are presented in the Supporting Information).

$$e^{a,v}(x,y,z,C) = \sum_{L=1}^{L=2}\int_{\varphi_{min}}^{\varphi_{max}}\int_{\Theta_{min}}^{\Theta_{max}}\frac{P_{\lambda,L}}{2\pi^2 R_L Z_L}\frac{A_c}{V_c}T_{EPR-gl,\lambda}\,a_{s,\lambda}(C,y)\sin^2\varphi\, sin\Theta\, d\varphi d\Theta \quad (23)$$

Where A_c, V_c and C are the superficial area of the cell (x,z-Plane), the cell volume and the suspension concentration in the cell, respectively. The optical properties of the EPR glass cell ($T_{EPR-gl,\lambda}$) and the catalyst suspension $a_{s,\lambda}(C,y)$ were determined from spectral transmittance measurements (Fig. S2). The average values of the local volumetric rate of photon absorption are reported in Table S3.

4. Results and discussion

The analysis of the reaction mechanism and kinetics of any catalytic reaction requires a multitechnique approach. Starting with the mechanism, here we make use of a combination of DRIFTS and EPR to support the mechanism summarized in Table 2. More precisely, while we cannot provide a complete description of the mechanism, the utilization of these two techniques aims to provide important, qualitative information to sustain the main steps of the reaction mechanism.

The DRIFTS study shows in the upper panel of Fig. 3 the initial sample spectrum and a difference one obtained after saturation with the pollutant (in the reactive mixture) and having as reference the initial sample spectrum included in panel A of Fig. 3. Apart from differences in the OH/water region, we can see the characteristics C-H (ca. 2900-2700 cm^{-1}) and C-C/C=O (below 1700 cm^{-1}) frequencies of the acetaldehyde molecule.[41,42,43] In the central panel of Fig. 3 we show difference spectra under reaction conditions, taking as reference the one obtained at t=0 after light switching on. The Supporting Information section contains a plot of the intensity behaviour of the IR signals observed during the experiment (Fig. S5).

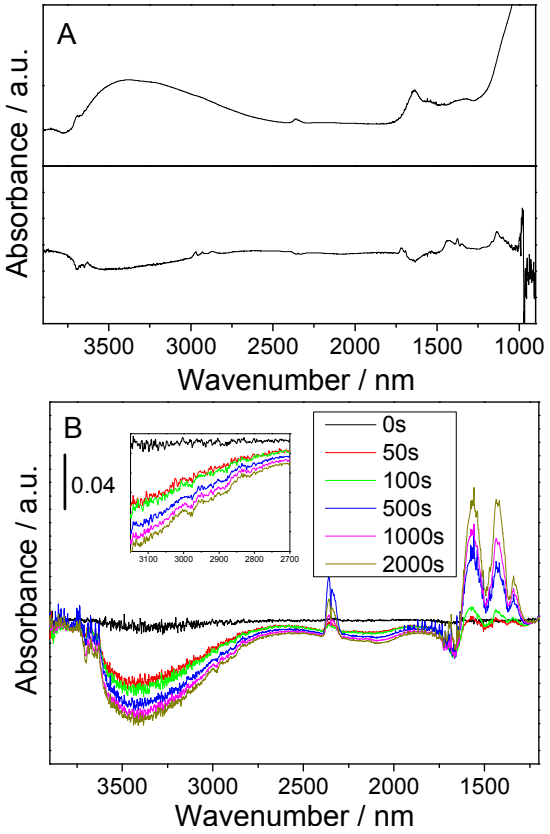

Fig. 3. IR spectra of the 0.025CeO_2/TiO_2 sample subjected to reaction conditions as in photocatalytic experiments. (A) Initial spectra and difference spectra after saturation with the pollutant. (B) Time-resolved spectra under UV illumination. (C) Comparison of light on-off-on spectra at the end to the experiment.

The presence of peaks below ca. 2990 (weak contributions at ca. 2990, 2955 and 2850 cm^{-1}, detected over negative ones ascribed to acetaldehyde –see inset in Fig. 3B), 1575 (strong), 1435 (strong), and 1339 (strong) cm^{-1} appears immediately. These are ascribable to acetate and formate species, produced by photo-oxidation of acetaldehyde.[43,44] The formation of these species is detected in parallel to the growth of the gaseous CO_2 signal at ca. 2350 cm^{-1}, indicating the progress of the photo-oxidation up to total

mineralization, as well as a concomitant elimination or displacement (from the surface) of water and/or hydroxyls (negative broad signal, 3500-2700 cm^{-1}).[45] Carbonate/bicarbonate species would not be present during reaction due to absence of signals in the 1300-1100 cm^{-1} interval.[46] At higher reaction times we nevertheless observed a single band at ca. 1690 cm^{-1} indicative of acetone or oxalate species.[41,44,47] Importantly, the lower panel of Fig. 3 displays a switching on-off-on experiment of the light source carried out (as demonstrated in Fig. S5) at nearly steady-state conditions for surface coverage. It strongly indicates that all detected absorbed species are not kinetically relevant intermediates of the reaction as they do not suffer any detectable effect under light changes although they are obviously connected with the steady state kinetics. The study presented in Fig. 3 is representative of the two illumination conditions tested as no significant differences were encountered between both. Thus, the study strongly suggests that once acetaldehyde is adsorbed in the catalyst surface, it is ready transformed with significant relevant steps only at the starting of the reaction, before formation of acetate/formate species (the early detected surface species after illumination). Table 2 interprets this fact neglecting the importance of chemical steps after the radical attack to the pollutant. As discussed below, this last key step will be analysed with EPR. Specifically, we will show the significance of OH-related radicals as proposed in Table 2.

To analyse the kinetic behaviour of the CeO_2-TiO_2 composite material, apart from the mechanism, we must consider the optical properties, and more precisely, the photon absorption properties. Both informations are combined in Eq. 12 to render an ab initio description of the photocatalytic properties of $0.025CeO_2/TiO_2$. In Fig. 4 we present the LSRPA for $0.025CeO_2/TiO_2$ and the TiO_2-reference samples for all illumination conditions tested in this work. For the ceria concentration used, we observed a moderate effect under both UV and visible excitation with respect to the titania reference (for a ceria loading of 2.5 mol. %, the increase in surface photon absorption rate is mostly observed in the visible region).[17,20,31] It would be thus expected a moderate influence in the kinetic performance of the CeO_2-TiO_2 composite sample. Note that such influence is dismissed in usual Langmuir-Hinshelwood or other simplified mechanisms customarily used to describe photocatalytic reactions.

Eq. 1 was solved numerically using MATLAB® R2010b with a nonlinear least-squares fitting algorithm (lsqnonlin, Algorithm: Trust-Region-Reflective Optimization).[48] Numerical analysis of Eq. 1 indicates that, under the operating conditions of the experiments, the term $K_{CH_3CHO}C_{CH_3CHO}$ was at least three orders of magnitude lower than 1 and can be neglected from Eq. 12. Similar situations have been observed in other photo-oxidation reactions of organic pollutants.[31,49]

The outcome of the kinetic modelling (Eq. 24) renders thus three constants (α_1, α_2, K_{H_2O}) presented in Fig. 5 and results of the parametric fitting are summarized in Table 3.

$$r_{CH_3CHO} = -\frac{\alpha_1 C_{CH_3CHO} C_{H_2O}}{(1+K_{H_2O}C_{H_2O})(1+\alpha_2 C_{CH_3CHO}+K_{H_2O}C_{H_2O})}\sqrt{e^{a,s}} \quad (24)$$

Fig. 5 also provides evidence (first panel) of the goodness of the fitting, with a root mean square error lower than ca. 7 % for all samples (Table 3). Fig. 5 also presents a few sections of the hyperpotential surface of the concentration at the outlet of the reactor as a function of the three main variables, pollutant initial concentration, humidity and irradiation intensity. Such sections show the relatively smooth variation of the rate as a function of the experimental variables.

Importantly, Table 3 can allow quantifying ceria effect on titania thorough the analysis of the kinetic parameters. To this end, i.e. to obtain physical insight of the photo-elimination key variables, from the kinetic study we extract the here called alpha parameter, defined as the ratio between kinetic parameters as follows:

$$\alpha = \frac{\alpha_1}{\alpha_2 K_{H_2O}} = \sqrt{\frac{\overline{\Phi}}{k_3}}k_1\,[Sites] \quad (25)$$

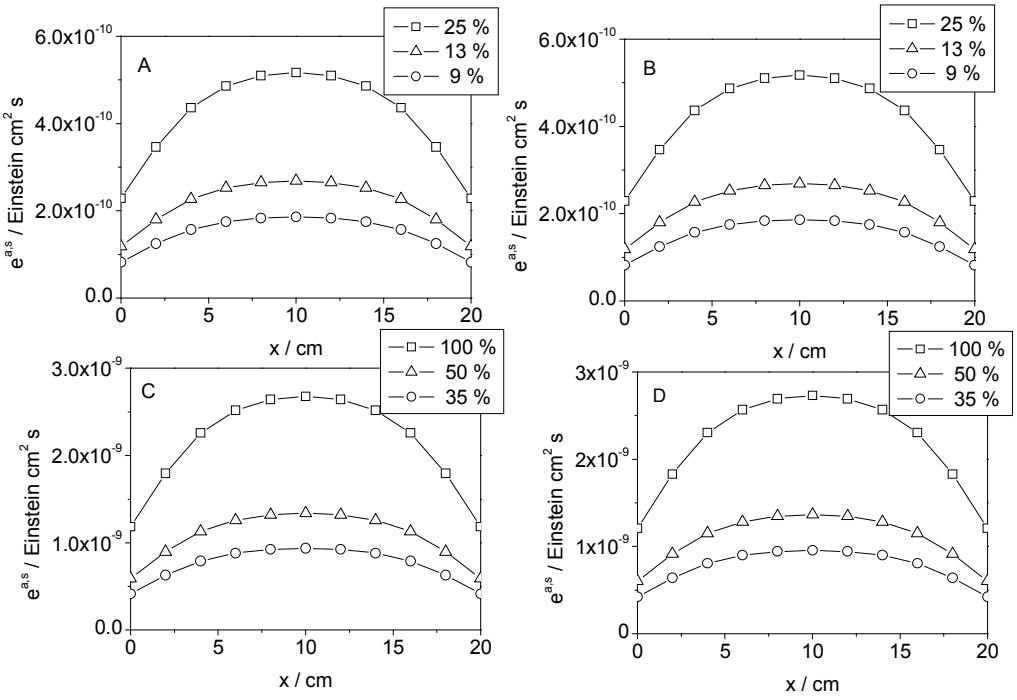

Fig. 4. Local surface rate of photon absorption along of x coordinate under UV and Visible irradiation with the different optical filters used. (A) TiO_2-UV, (B) $0.025CeO_2/TiO_2$-UV, (C) TiO_2-VIS, (D) $0.025CeO_2/TiO_2$-VIS.

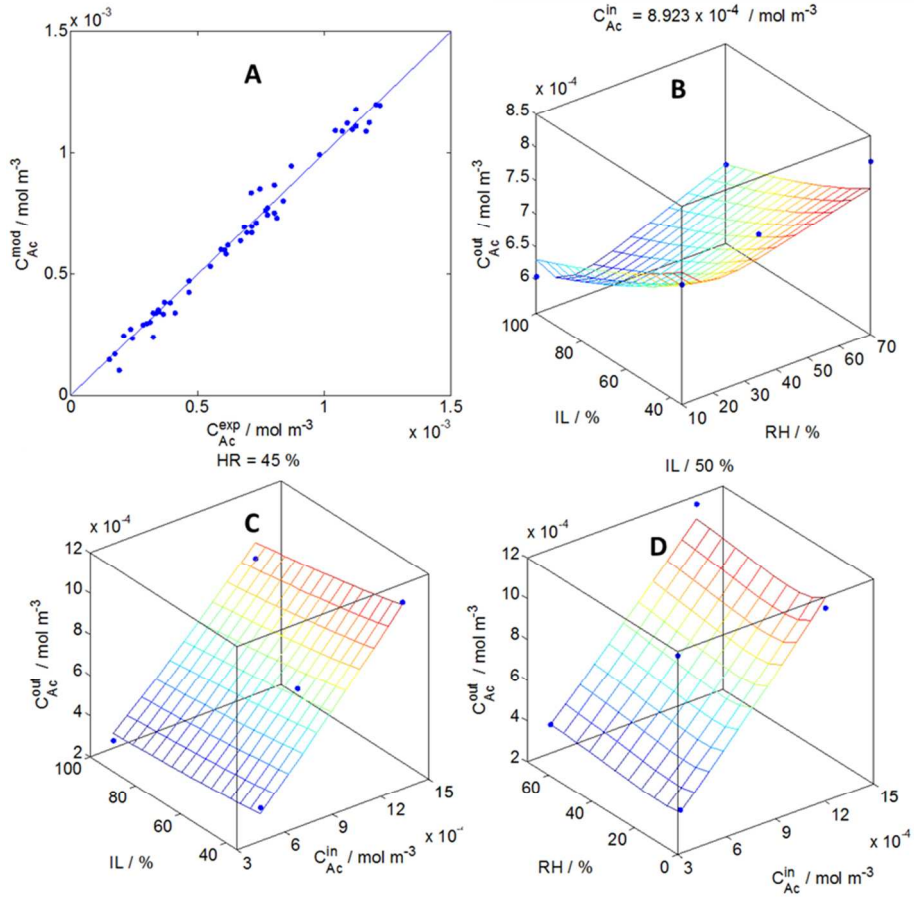

Fig. 5. A. Experimental values against model predictions of Acetaldehyde concentration for samples and different operating conditions. B, C and D. Model (Surface) and experimental results (points) for $0.025CeO_2/TiO_2$ sample under visible irradiation. IL: Irradiation Level; HR: relative humidity; and C_{Ac}^{in}, C_{Ac}^{out}: Initial and final acetaldehyde concentration, respectively.

Table 3. Values of the kinetic parameters

Parameters	**TiO_2** UV	**TiO_2** VIS	**$0.025CeO_2/TiO_2$** UV	**$0.025CeO_2/TiO_2$** VIS
$\boldsymbol{\alpha_1}$ $\left[\mathbf{Einstein^{-1/2}s^{-1/2}\ m_{sup}^{-1}(m_{air}^3)^2}\right]$	1.6×10^{-2}	4.6×10^{-3}	2.9×10^{-2}	4.9×10^{-3}
$\boldsymbol{\alpha_1}$ error	3.5×10^{-3}	1.8×10^{-3}	6.9×10^{-3}	2.1×10^{-3}
$\boldsymbol{\alpha_2}$ $\left[\frac{\mathbf{mol}_{CH_3CHO}}{\mathbf{m_{air}^3}}\right]$	4.3×10^3	4.3×10^3	4.2×10^3	3.3×10^3
$\boldsymbol{\alpha_2}$ error	1.0×10^3	2.3×10^3	1.2×10^3	1.7×10^3
$\boldsymbol{K_{H_2O}}$ $\left[\frac{\mathbf{mol}_{H_2O}}{\mathbf{m_{air}^3}}\right]$	9.2	9.2_5	7.5	6.8
$\boldsymbol{K_{H_2O}}$ error	3.0	3.5	2.0	1.6
$\boldsymbol{\alpha}$ $\left[\mathbf{mol}_{CH_3CHO}\ \mathbf{Einstein^{-1/2}s^{-1/2}\ m_{sup}^{-1}}\right]$	4.1×10^{-7}	1.1×10^{-7}	9.2×10^{-7}	2.2×10^{-7}
$\boldsymbol{\alpha}$ error	1.8×10^{-7}	8.8×10^{-8}	4.2×10^{-7}	1.5×10^{-7}
RMSE [%]	2.9	2.8	6.9	4.5

Table 4. Values of $r_{OH^\bullet}$ obtained by EPR measurements

	TiO_2 UV	TiO VIS	$0.025CeO_2/TiO_2$ UV	$0.025CeO_2/TiO_2$ VIS
$r_{OH^\bullet}$ $\left[\frac{\text{Number of spins } (OH^\bullet)}{cm^3 s}\right]$	8.7	3.1	23.4	4.4
$rOH^\bullet$ error	2.6	0.8	2.7	1.1

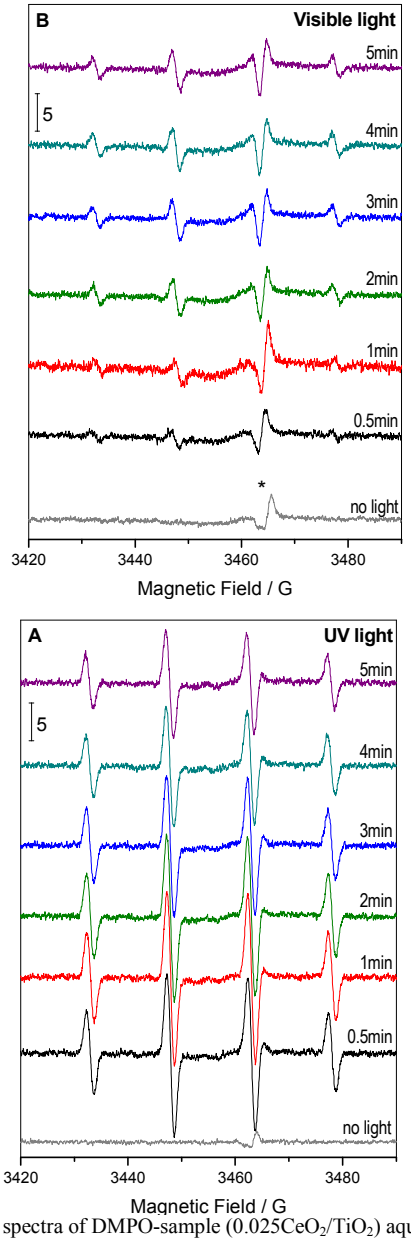

Fig. 6. EPR spectra of DMPO-sample ($0.025CeO_2/TiO_2$) aqueous suspension as a function of irradiation time; (A) UV; (B) visible light. The asterisk marks a residual paramagnetic impurity at the cavity.

The alpha parameter values for the samples here analysed are included, as mentioned, in Table 3. The analysis of alpha in a large Ce-Ti series of samples having growing quantities of ceria in contact with the same titania-anatase nanophase showed the dominance of the $k_1/\sqrt{k_3}$ term.[17] Thus, as the comparative analysis with EPR results will also indicate here, the alpha parameter variation though a sample series will render information about two elemental steps with kinetic constants k_1 and k_3. Step one (k_1) is the creation of hole-related radicals while step 3 (k_3) accounts for the annihilation of hole-related radicals. We note that the number of adsorption sites in Eq. (25) is reasonably constant among the samples series studied as they would be located at the most active anatase surface, the phase that account for 97.5 mol % at the composite catalyst. The alpha parameter is thus extremely insightful about the availability of hole-related radical species attacking the pollutant during reaction.

In parallel and as a spectro-kinetic tool, we use EPR to track the number of OH-radical species at the surface of the $0.025CeO_2/TiO_2$ sample and TiO_2 reference under the two illumination conditions tested. With the help of the DMPO trapping molecule we measured the time evolution of the $OH^\bullet$, hole-related radical species (see Fig. 6 for experimental data corresponding to the $0.025CeO_2/TiO_2$ sample). Both UV and visible irradiation of DMPO-containing sample suspensions gives rise to a signal with 1:2:2:1 intensity pattern for all samples. Its EPR parameters (g = 2.0056, a_N= 14.9 G, a_H = 14.9 G) are characteristic of DMPO-OH adducts and measured the formation of $OH^\bullet$ radicals.[50,51,52]

A comparison of the initial rate of $OH^\bullet$ for the first minutes (before multiple additions, within consecutive reactions, of $OH^\bullet$ radicals to the spin trapping molecule would drive to the formation of diamagnetic species) is customarily used to compare the sample power to generate this radical species.[53,54,55] Fig. 6 indicates that the initial rate is always defined in the first 2-3 minutes of the EPR experiment. According to Eq. 22, the EPR measurement described a similar physical magnitude than the alpha parameter described in Eq. 25. The single difference is related to the adsorbed water concentration presents in Eq. 22 but as EPR measurements are carried out at constant unitary coverage (i.e. saturation) this would influence to a little extent the comparison of the two measurements when comparing the $0.025CeO_2/TiO_2$ sample with the TiO_2 reference.

From the above discussion it becomes evident that either we can use EPR or kinetic analysis to measure the same physical observable described in the corresponding equations (Eqs. 22 and 25). The results of the kinetic and EPR analyses are summarized in Tables 3 and 4, respectively. In Fig. 7 we plot both normalized experimental observables as a function of the normalized (per surface area) reaction rate with a two-fold aim. First, it is a check of consistency of both approaches and an interpretation of the measurements. In fact the good correlation between the two set of variables measuring similar physical quantities indicates that the common factor to all samples, i.e. $k_1/\sqrt{k_3}$ dominates the trend in Fig. 7 and, on the other hand, is reasonably measured (within experimental error) using these two independent procedures. The second and more important aim is that the plot, and particularly the EPR results, shows that the normalized rate is proportional to the availability of holes at the surface of the CeO_2-TiO_2 catalyst. This confirms the hole-mediated radical mechanism proposed in Table 2 as a key kinetic step and also points out the main role of CeO_2 in the composite material. Interesting to note is that the two conclusions mentioned hold both for UV and visible light illumination. As far as we know, this is the first time that this reaction has been shown to be triggered by a kinetically-relevant hole radical attack irrespective of the illumination wavelength in the UV-visible electromagnetic range.

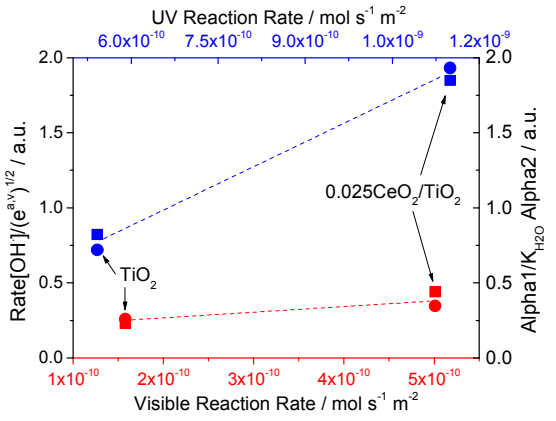

Fig. 7. Correlation plot of the normalized kinetic parameter ratio (Squares) and the normalized rate of $OH^{\bullet}$ related radical formation (Circles) vs. the reaction rate for the Ti and 0.025CeTi samples. Blue: UV irradiation Red: Visible irradiation. Normalization parameters: $\left(\frac{\alpha_1}{\alpha_2 K_{H_2O}}\right) 2 \times 10^6$; $\left(\frac{r_{OH^{\bullet}}}{\sqrt{e^{a,v}}}\right) 1.25\times10^{-4}$.

Ceria is thus promoting an "effective" charge separation after light excitation and leaves holes available for chemical reaction at the surface of the $0.025CeO_2/TiO_2$ catalyst. We stress again that this physical effect occurs both under UV and visible light illumination conditions, indicating the general validity of the promotion mechanism as well as the suitability of the material to boost titania activity under sunlight, a green energy source for decontamination reactions. To further progress in the analysis of the promotion effect, we can compare the slope of the lines going from the TiO_2 reference to the $0.025CeO_2/TiO_2$ sample in Fig. 7. This would provide a semi-quantitative estimation of such effect under the two illumination conditions tested. The ratio between the UV and visible slopes ca. 3.2, clearly indicates that a more favourable situation is encountered in the UV case.

The interpretation of the differential effect under UV and visible light might be explained on the basis of previous works.[17,18,56] The valence and conduction band edges position of our ceria and titania do not allow an efficient charge handling or separation after light excitation. The corresponding band levelling would favour the transfer of the two charge carriers (electrons and hole) to the relatively inefficient (with respect to titania) ceria surface.[57] Thus, the main role of ceria has been shown to be related to the capture of electrons, in turn related to the presence of oxygen defects. Such oxygen defects are shown to be promoted by the presence of titania in larger quantities than the corresponding to the (same size) ceria nanoparticle, and are preferentially located at the ceria-titania interface.[17,56] Such defects are expected to have a relatively wide energy distribution which, based on current results, would promote a more efficient capture of UV excited electrons simply by energetic and/or more complex (like kinetics of charge trapping) reasons, in turn related to specific surface positions (for example as corners of ceria entities) and/or the chemical nature of the vacancies (typically isolated vs. associated centers). Further analysis would be required to fully interpret the situation although the situation cannot be easily evaluated as it is predicable that a specific analysis of ceria-titania interface defects (and not all ceria-related defects) must be required to interpret the situation. For example, their physical location would complicate the use of probe molecules (together with IR and/or EPR techniques) to evaluate their properties.

5. Conclusions

A $0.025CeO_2/TiO_2$ photocatalyst with a 2.5 mol. % of ceria was used in the photo-oxidation of acetaldehyde. The study was focused on analysing the key steps of the reaction in order to interpret the promoting effect of ceria on anatase. To do it, we carried out a combined spectroscopic and kinetic approach.

The behaviour of the $0.025CeO_2/TiO_2$ photocatalyst was thus interpreted with the help of a single TiO_2 reference through the analysis of the reaction mechanism and kinetics, the latter with explicit inclusion of the light in the corresponding conceptual framework. The combination of spectroscopic and kinetic studies allows the settlement of a self-consistent approach that simultaneously validates the kinetic approach and analyses the roots of the photoactivity behaviour of the CeO_2-TiO_2 composite sample. In this way it is shown that photoactivity is governed by the surface reaction between hole-derived radicals and the pollutant. The role of ceria in the composite catalyst is mainly related to the promotion of charge carrier separation after light excitation. The OH-radical attack to the pollutant is shown to be important and kinetically determinant under both UV and visible light illumination conditions, driving thus activity irrespective of the excitation wavelength, indicating the excellent capabilities of the CeO_2-TiO_2 system for sunlight photocatalytic applications.

Acknowledgements

A. Kubacka and M.J. Muñoz-Batista thank MINECO for support thought, the postdoctoral "Ramón y Cajal" programs and predoctoral FPI and, respectively. M. J. Muñoz-Batista would like to thank MINECO for a grant-in-aid (EEBB-I-13-06684) allowing his stay at Santa Fe, Argentina. Financial support by MINECO is also acknowledged (project CTQ2010-14872/BQU). Also, the authors acknowledge financial support from the Universidad Nacional del Litoral, Agencia Nacional de Promoción Científica y Tecnológica, and Consejo Nacional de Investigaciones Científicas y Técnicas of Argentina. A.C. Negro is also thanked for measurements on Optronic spectroradiometer.

Notes and references

[a] Instituto de Catálisis y Petroleoquímica, CSIC, C/Marie Curie 2, 28049-Madrid, Spain.

[b] Instituto de Desarrollo Tecnológico para la Industria Química (INTEC, UNL- CONICET), Güemes 3450, 3000, Santa Fe, Argentina.

† Corresponding authors emails: O.M.A .(alfano@intec.unl.edu.ar), A.K. (ak@icp.csic.es)

Electronic Supplementary Information (ESI) available: details of the photocatalytic experiments, EPR cell geometry, optical and infrared measurements, integration limits of equations Eqs. 18 and 23 of the main text as well as analysis of internal and external mass transfer. See DOI: 10.1039/b000000x/

1 S. Wang, H.M. Ang, M.O. Tade, *Environ. Int*., 2007, **33**, 694.
2 M.R. Hoffmann, S.T. Martin, W. Choi, D.W. Bahnemann, *Chem. Rev.,* 1995, **95**, 69.
3 R. Vinu, G. Madras, *J. Indian Inst. Sci*., 2010, **90**, 189.
4 A. Kubacka, G. Colón, M. Fernández-García, *Chem. Rev*., 2012, **112**, 1555.
5 O. Carp, C.L. Huisan, A. Reller, *Prog. Solid State Chem*., 2004, **32**, 33.
6 C.W. Lai, J.C. Juan, W.B. Ko, S.B.A. Hamid, *Int. J. Photoenergy*, 2014, 524135-6.
7 S. Parasupree, Y. Suzuki, S. Prisa-Art, S. Yoshikawa, *S. J. Sol. St. Chem*., 2005, 178, 128.
8 T. Tong, J. Zhang, B. Tian, F. Chen, D. He, M. Anpo, *J. Colloid Interf. Sci*., 2007, **315**, 382.
9 G. Li, D. Zhang, Y.C. Yu, *Phys. Chem. Chem. Phys.,* 2009, **11**, 3775.
10 V. Stengl, S. Bakardejieva, N. Murafa, *Mater. Chem. Phys*., 2009, **114** 217.
11 R. Sasikala, A.R. Shirole, V. Sudarsan, V.S. Kamble, C. Sudarkar, R. Naik, R. Rao, S.R. Bharawaj, *Appl. Catal. B: Environ*., 2010, **390**, 245.
12 H. Lin, M. Wang, Y. Wang, Y. Liang, W. Cao, Y. Su, *J. Photochem. Photobiol. A,* 2011, **223**, 157.
13 A.A. Ismail, H. Bouzid, *J. Colloid Int. Sci*., 2013, **404**, 127.
14 Y. Wang, B. Li, C. Zhang, L. Cui, S. Kang, X. Li, L. Zhou, *Appl. Catal. B: Environ*., 2013, **130–131**, 277.
15 Y. Liu, P. Fang, Y. Cheng, Y. Gao, F. Chen, Z. Liu, Y. Dai, *Chem. Eng. J.*, 2013, **219**, 478.
16 C. Karunakaran, P. Gomathisankar, *ACS Sus. Chem. Eng.*, 2013, **1**, 1555.
17 M.J. Muñoz-Batista, M.N. Gómez-Cerezo, A. Kubacka, D. Tudela, M. Fernández-García, *ACS Catal*., 2014, **4**, 63.
18 M.J. Muñoz-Batista, M. Ferrer, M. Fernández-García, A. Kubacka, *Appl. Catal. B: Environ*., 2014, **154-155**, 350.
19 X. Sun, C. Li, L. Ruan, Z. Pen, J. Zhang, Y. Li, *J. Alloys Comp*., 2014, **585**, 800.
20 M.J. Muñoz-Batista, M.M. Ballari, A. Kubacka, E.A. Cassano, O.M. Alfano, M. Fernández-García, *Chem. Eng. J.*, 2014, **255**, 297.
21 M.L. Sauer, D.F. Ollis, *J. Catal*., 1996, **158**, 570.
22 V. Augugliaro, M. Bellardita, V. Loddo, G. Palmisano, L. Palmisano, S. Yurdakat, *J. Photochem. Photobiol.C*, 2012, **12**, 224.
23 O.M Alfano, D Bahnemann, A.E Cassano, R.Dillert, R.Goslich, *Catal.. Today*, 2000, **58**, 199.
24 A. Kubacka, G. Colón, M. Fernández-García, *Appl.Catal. B: Environ.,* 2010, **95**, 238.
25 Y. Wu, J. Zhang, L. Xiao, F. Chen, *Appl. Surf. Sci.*, 2010, **256**, 4260.
26 Y. Niu, M. Ying, J: Zhang, B. Tian, *Catal. Today,* 2013, **201**, 159.
27 P.G. De Gennes, C. Taupin, *Journal of Physical Chemistry*, 1982, **86** 2294.
28 A. Kubacka, B. Bachiller-Baeza, G. Colón, M. Fernández-García, *Appl.Catal. B: Environ*., 2010, **93,** 274.
29 G. E. Imoberdorf, H. A. Irazoqui, A. E. Cassano, O. M. Alfano, *Ind. Eng. Chem. Res.*. 2005, **44**, 6075.
30 C. Passalía, M. E. M. Retamar, O. M. Alfano, R. J. Brandi*, Int. J. Chem. React. Eng.,* 2010, **8**, 1.
31 M. J. Muñoz-Batista, A. Kubacka, M. N. Gómez-Cerezo, D. Tudela, M. Fernández-García. *Appl. Catal. B: Environ*., 2013, **140–141**, 626.
32 M.M. Ballari, M. Hunger, G. Hüsken, H.J.H. Brouwers, *Catal. Today*, 2010, **151**, 71.
33. Y. Ohko, D. A. Tryk, K. Hashimoto, A. Fujishima, *J. Phys. Chem. B*, 1998, **102**, 2699.
34 M. L. Sauer, D. F. Ollis, *J. Catal*, 1996, **158**, 570.
35 D.W. Bahnemann, M. Hilgendorff, R. Memming, *J. Phys. Chem. B*, 1997, **101**, 4265.
36 G.L. Chiarello, D. Ferri, E. Selli, *J. Catal*., 2011, **280**, 168.
37 M. G. Gonzalez, E. Oliveros, M. Wörner, A. M. Braun, *J. Photochem. Photobiol. C,* 2004, **5**, 225.
38 G. Vella, G.E. Imoberdorf, A. Sclafani, A.E. Cassano, O.M. Alfano, L. Rizzutia, *Appl. Catal. B: Environ*., 2010, **96**, 399.
39 D. K. Edwards, *Solar Energy*, 1977, **19**, 401.
40 M. B. Marcó, A. d. L. Quiberoni, A. C. Negro, J. A. Reinheimer, O. M. Alfano. *Chem. Eng. J*., 2011, **172**, 987.
41 T. Berger, M. Sterner, O. Diwald, E. Knozinger, D. Panaychoro, F.L. Thompson, *J. Phys. Chem. B,* 2005, 109, 6061.
42 C. Lamberti, A. Zecchina, E. Groppo, S. Bordiga, *Chem. Soc. Rev*., 2010, **39**, 4951.
43 Z. Topalian, B.I. Stefanov, C.G. Granqvist, L. Österlund, *J. Catal.*, 2013, **307**, 265.
44 M.D. Hernández-Alonso, I. Tejedor, J.M. Coronado, M.A. Anderson, J. Soria, *Catal. Today*, 2009, **143**, 364.
45 G. Colón, M.C. Hidalgo, J.A. Navío, A. Kubacka, M. Fernández-García, *Appl. Catal. B: Environ*., 2009, **90**, 633.
46 L. Mino, G. Spoto, A.M. Ferrari, *J. Phys. Chem. C*, 2014, in press, doi: 10.1021/jp507443k.
47 I. Dolamina, T. Burghi, *J. Catal*., 2007, **248**, 268.
48 T.F. Coleman, Y. Li, *SIAM J. Optimization,* 1994, **6**, 418.
49 M.L. Satuf, R.J. Brandi, A.E. Cassano, O.M. Alfano, *Appl. Catal. B: Environ*., 2008, **82**, 37.
50 M.A. Grela, M.E.J. Coronel, A.J. Colussi, *J. Phys. Chem*., 1996, **100**, 16940.
51 E. G. Janzen, N. Sankuratry, Y.Kotake, *J. Magn. Reson*., 1996, 111, 254.

52 A. Kubacka, M. Ferrer, A. Martínez-Arias, M. Fernández-García, *Appl. Catal. B: Environ*., 2008, **84**, 87.
53 A. Kubacka, M. Muñoz-Batista, M. Ferrer, M. Fernández-García, *Appl. Catal. B: Environ.,* 2013, **140-141**, 680.
54 Q. Chen, H. Shi, W.S. Li, Y. Xu, D.W. Wu, *Catal. Sci. Technol*,, 2012, **2**, 1213.
55 M.J. Muñoz-Batista, A. Kubacka, R. Rachwalick, B. Bachiller-Baeza, M. Fernández-García, *J. Catal*. 2014, **309**, 428.
56 A.C. Johnston-Peck, S.D. Senanayake, J.J. Plata, S. Kundu, W. Xu, L. Barrio, J. Graciani, J.F. Sanz, R.M. Navarro, J.L.G. Fierro, E.A. Starch, J.A. Rodriguez, *J. Phys. Chem. C*, 2013, **117**, 14463.
57 Y. Xu, M.A.A. Schoonen, *Am. Mineral*., 2000, **85**, 543.